Volume 4 | Number 1 | January 2019 | Pages 1–244

Nanoscale Horizons

The home for rapid reports of exceptional significance in nanoscience and nanotechnology

rsc.li/nanoscale-horizons

ISSN 2055-6756

ROYAL SOCIETY OF CHEMISTRY | Celebrating IYPT 2019

REVIEW ARTICLE
Wei Wu *et al.*
NIR light-activated upconversion semiconductor photocatalysts

NCNST

Nanoscale Horizons

REVIEW

View Article Online
View Journal | View Issue

Cite this: *Nanoscale Horiz.*, 2019, 4, 10

NIR light-activated upconversion semiconductor photocatalysts

Qingyong Tian,†[ab] Weijing Yao,†[a] Wei Wu *[ac] and Changzhong Jiang[a]

Received 2nd July 2018,
Accepted 13th August 2018

DOI: 10.1039/c8nh00154e

rsc.li/nanoscale-horizons

Harvesting of near infrared (NIR) light in the abundant and environmentally friendly solar spectrum is particularly significant to enhance the utilization rate of the cleanest energy on earth. Appreciating the unique nonlinear optical properties of upconversion materials for converting low-energy incident light into high-energy radiation, they become the most promising candidates for fabricating NIR light-active photocatalytic systems by integrating with semiconductors. The present review summarizes recent NIR light-active photocatalytic systems based on a sequence of $NaYF_4$-based, fluoride-based, oxide-based and Ln^{3+} ion-doped semiconductor-based photocatalysts for degradation of organic molecules. In addition, we provide an in-depth analysis of various photocatalytic mechanisms and enhancement effects for efficient photo-redox performance of different upconversion semiconductor photocatalysts. We envision that this review can inspire multidisciplinary research interest in rational design and fabrication of efficient full-spectrum active (UV-visible-NIR) photocatalytic systems and their wider applications in solar energy conversion.

1. Introduction

Currently, steadily worsening environmental pollution is an overwhelming global crisis that threatens the health of human beings and sustainable development of natural ecosystems. To solve these urgent issues, the exploitation of green and environmentally friendly technologies for alternative energy conversion and environmental remediation is proven to be an imperative requirement.[1] Among the various approaches, photocatalysis is valuable for environmental protection and remediation of contaminants as it can efficiency utilize the solar spectrum or artificial light sources, and thus lead to virtually unlimited energy source all over the world.[2–5] Especially, semiconductor-based photocatalysts such as TiO_2, ZnO, SnO_2, *etc.*, have been widely applied in photodegradation and photo-oxidization of hazardous organic molecules.[6–9] The initial explanation of n-type TiO_2 electrode in 1972 by Fujishima and Honda (Honda–Fujishima effect) was a significant milestone for semiconductor photocatalysis.[10] And the first description

[a] *School of Printing and Packaging and School of Physics and Technology, Wuhan University, Wuhan 430072, P. R. China. E-mail: weiwu@whu.edu.cn; Fax: +86-27-68778433; Tel: +86-27-68778529*
[b] *College of Materials Science & Engineering, Zhengzhou University, Zhengzhou 450052, P. R. China*
[c] *Suzhou Research Institute of Wuhan University, Suzhou 215000, P. R. China*
† Contributions are equal.

Qingyong Tian

Qingyong Tian received his BS degree at Hubei University in 2013. He is currently pursuing a PhD degree under the supervision of Prof. Changzhong Jiang and Prof. Wei Wu in the School of Physics and Technology at Wuhan University. His research focuses on the design and synthesis of multi-functional nanostructured materials for applications in photocatalysts and advanced energy devices.

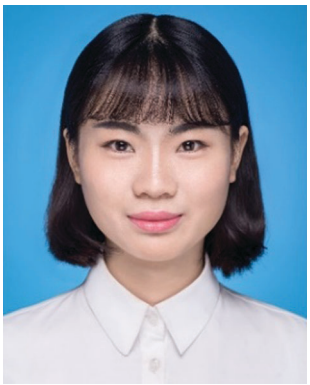

Weijing Yao

Weijing Yao received her BS in 2015 from Inner Mongolia Agricultural University. She is currently pursuing a PhD degree under the supervision of Prof. Wei Wu in the School of Printing and Packaging at Wuhan University. Her research involves the design and synthesis of upconversion materials for anti-counterfeiting applications.

of TiO_2 suspension for the photodegradation of polychlorinated biphenyl and cyanide by Cary and Bard in 1980 opened a new gate for TiO_2-based semiconductors for the elimination of environmental pollution.[11,12] TiO_2 possesses the advantages of cost-effectiveness and pollution-free and sustainable development and has been widely investigated in recent decades. However, the wide bandgap of TiO_2 (>3.0 eV) has been a major limitation for efficient utilization of solar photons.[13–15] The light absorption threshold is confined in the ultraviolet (UV) region (300–400 nm), which only accounts for 5% of the full spectrum. Therefore, the losses in solar conversion efficiency have resulted in under-utilization of visible (43%, 400–700 nm) and NIR light (52%, 700–2500 nm). Narrow bandgap semiconductors, such as CdS, Fe_2O_3, g-C_3N_4, *etc.*, could broaden the absorption threshold to the visible region and demonstrate efficient photocatalytic performance.[16,17] NIR-light-active semiconductors with narrower bandgap could further absorb NIR light, while the lower-lying conduction band (CB) and higher-lying valence band (VB) present fairly inert photodecomposition or photo-oxidization abilities to organic dyes. Carbon quantum dots (CQDs) with both up- and down-converted photoluminescence (PL) and photoinduced electron transfer ability could give rise to intense absorption of NIR light.[18,19] The surface plasmon resonance (SPR) peaks of noble-metal plasmonic nanoparticles can be red-shifted to the NIR region by rational adjustment of sizes, morphologies and alloying compositions.[20,21] Their tunable optical characteristics make CQDs and noble-metal plasmonic nanoparticles alternative co-catalysts to harvest NIR photons and enhance the NIR-induced photocatalytic performance. However, the inherent photocorrosion susceptibility and high processing cost make them far from practical propositions. Therefore, much effort should be made to introduce NIR light into semiconductor-based photocatalyst systems.[22,23]

One increasingly appealing and practical approach is coupling photocatalytic semiconductors with nonlinear optical materials that could utilize the abundant NIR light in photocatalysis, to improve the utilization of solar energy, and finally enhance the photoreactions.[24,25] Of especial note are the anti-Stokes luminescence mechanism-based upconversion materials, with the unique property to sequentially absorb two or multiple low-energy photons and radiate out specific types of photons with shorter wavelength, which are considered as potentially efficient candidates for exploitation of NIR excitation. Lanthanide ion (Ln^{3+})-doped upconversion materials with abundant f-orbital configurations have narrow fluorescence emission bands *via* intra-4f ($4f^n$–$4f^n$) or 4f–5d ($4f^n$–$4f^{n-1}5d$) orbital transitions.[26,27] The involved symmetries of inner electronic quantum states would yield metastable energy levels with long lifetimes that favor the incidence of successive populations in the energized states of Ln^{3+} ions. Under NIR laser irradiation, the pump photons in the ground state of sensitizer ions will be sequentially excited to the excited states of activator ions. Then, the population will relax non-radiatively or radiatively to the ground state of activator ions to achieve the upconversion emissions. The perfect shielding effect of outer 5s and 5p shells of Ln^{3+} prevents the influence of surrounding environment on electronic transitions, resulting in perfect physical and chemical stability against photobleaching and photochemical degradation. Doping with different Ln^{3+} ions in an inorganic substrate will induce designable upconversion emissions, from the UV, passing through the entire visible and extending to the NIR region under irradiation.[28–30] Fig. 1 presents the occupation of Ln^{3+} ion-doped upconversion materials with large absorption cross section for converting the NIR light in the solar spectrum into visible light. The main adsorption centers of the Ln^{3+} ions, *i.e.*, Nd^{3+}, Yb^{3+}, Ho^{3+} and Er^{3+}, are located at 808 (Nd^{3+}: $^4I_{9/2}$–$^4F_{5/2}$), 980 (Yb^{3+}: $^2F_{7/2}$–$^2F_{5/2}$), 1160 (Ho^{3+}: $^5I_8$–$^5I_6$)

Wei Wu

Wei Wu received his PhD in 2011 from the Department of Physics, Wuhan University, China. He then joined the group of Prof. Daiwen Pang at Wuhan University (2011) and Prof. V. A. L. Roy at City University of Hong Kong (2014) as a postdoctoral fellow. Now he is a full professor and Director of Laboratory of Printable Functional Nanomaterials and Printed Electronics, School of Printing and Packaging, Wuhan University. He has published over 80 papers, which have received over 3000 citations. He is also the topical editor of Frontiers in Materials. His research interests include the synthesis and application of functional nanomaterials, printed electronics and intelligent packaging.

Changzhong Jiang

Chang Zhong Jiang received his BS in 1983 from Huazhong University of Science and Technology and MS in 1990 from Wuhan University. He obtained his PhD in 1999 from Université Claude Bernard Lyon 1, France. He has been a full professor in the Department of Physics, Wuhan University since 2001, and he is also the Director of Center for Ion Beam Application, Wuhan University. He has published, as an author and co-author, more than 100 publications in various reputed international journals, such as Physical Review Letters, Nano Letters, ACS Nano, and Advanced Materials. His research interests include the synthesis and application of low-dimension nanomaterials, magnetic materials and ion beam modification of materials.

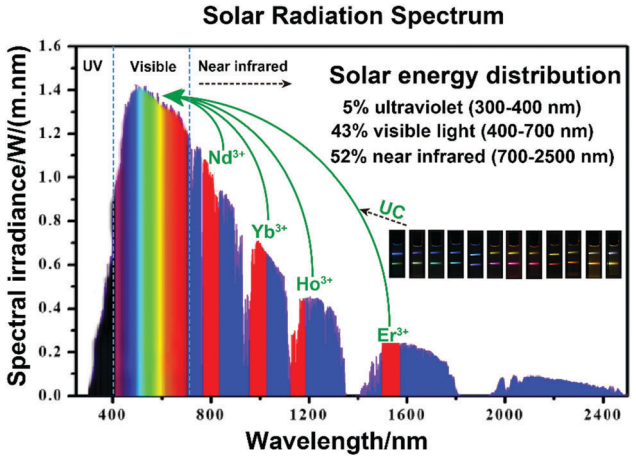

Fig. 1 The schematic conversion processing of NIR light into visible light *via* Ln^{3+} ions, referring to standard AM 1.5 solar radiation spectrum, and the tunable emissions of upconversion materials.

and 1530 (Er^{3+}: $^4I_{15/2}$–$^4I_{13/2}$) nm, respectively.[31] These ions will act as sensitizers that absorb the centered NIR photons and emit UV or visible photons through multiple photon absorption or energy transfer processes. For instance, tunable emissions varying from blue to red colors can be realized by fine-tuning the concentration of sensitizer Yb^{3+} ions and changing the doped activator Tm^{3+} and Er^{3+} ions.[32] The spectral power from the normalized air mass (AM) 1.5 spectrum yield is nearly 25 W m^{-2} ranging from 1480 to 1580 nm when Er^{3+} acts as the activator.[33] It will be extremely attractive to combine upconversion materials as frequency conversion elements with UV- or visible-active semiconductor photocatalysts to further harvest solar energy in a broader spectral range, and thus promoting the utilization of solar energy efficiently.

2. The Ln^{3+} ion-doped upconversion mechanism

The upconversion emissions are based on the transition of 4f electronic configurations between rare earth (RE) ions (Sc, Y and La are technically d-shield elements).[34] Each kind of RE ion has its definite energy level positions, and the upconversion processes between different RE ions are different from each other, while all of them represent similar property of chemical elements attributed to the dominant trivalent oxidation state. The characteristic energy level positions of different Ln^{3+} ions are illustrated in Fig. 2, which was well defined by experimental measurement by Dieke (Dieke diagram) and Carnall *et al.*[31,35] The energy level positions give detailed illustration of absorption and excitation spectra of Ln^{3+} ion-doped upconversion materials with distinguishable spectroscopic fingerprints. The upconversion process has been recognized to be grouped into three stages: excited state absorption (ESA), energy transfer (ET), and phonon avalanche (PA).

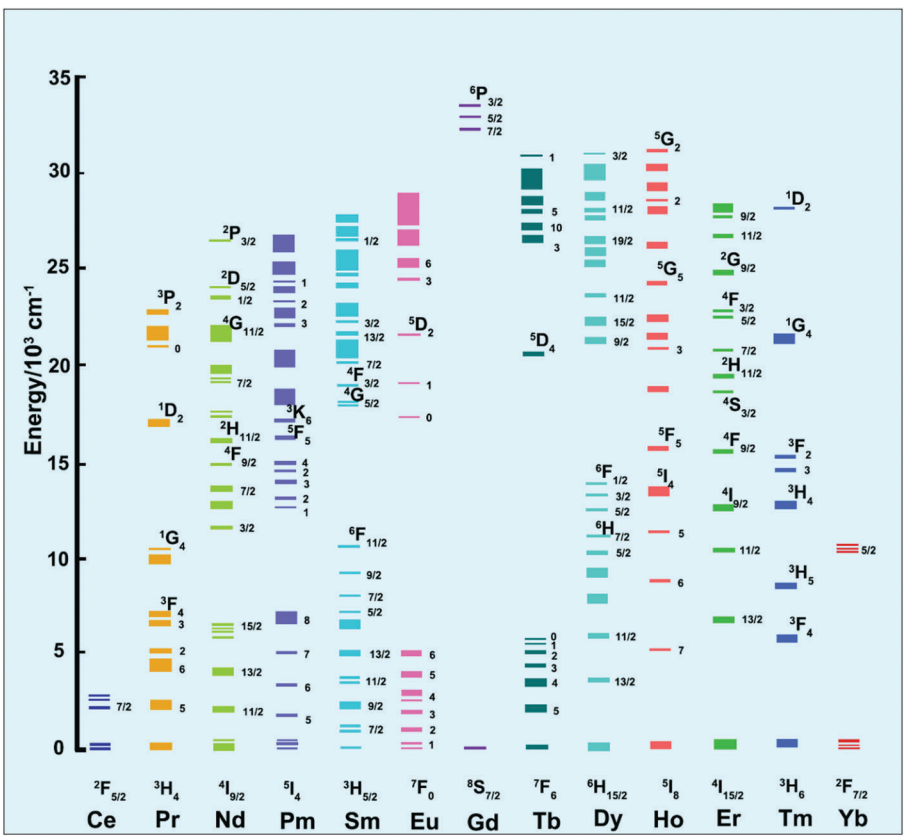

Fig. 2 Characteristic energy level positions of a sequence of Ln^{3+} ions.

2.1 Excited state absorption (ESA)

ESA is the basic process of upconversion luminescence first proposed by Bloembergen *et al.* in 1959.[36] The mechanism is that one type of Ln^{3+} ion is excited from the ground state (GS) to an excited state with high energy level through sequential two- or multiphoton absorption. Typically, as illustrated in Fig. 3a, the Ln^{3+} ion absorbed one photon hv_1 and is promoted from GS to intermediate metastable (electronic) state (E_1). Because of the long relaxation time of metastable energy level, the excited ions will stay or decay between the intra-band for a long time. And then, if another energy-matched photon matches the energy interval between E_1 and upper excited state E_2, the ions at state E_1 will absorb the photon energy and populate the state E_2, achieving successive absorption of two photons. Three or more multiphoton absorption processes will be deduced by analogy. Finally, the excited ions relax non-radiatively or radiatively to the GS, inducing the upconversion emissions. Additionally, supposing the incident photons are sequentially trapped by individual Ln^{3+} ions, then the upconversion efficiency of the ESA process is independent of the Ln^{3+} doping concentration. The usual doping concentration of Ln^{3+} ions is less than 1%.[37] Under continuous excitation, the intensity of upconversion luminescence (I_{uc}) is proportional to excitation power (I_{ex}):

$$I_{em} \propto (I_{ex})^n \quad (1)$$

where n is the number of pump photons.

2.2 Energy transfer upconversion (ETU)

The ETU process generally occurs between two types of ions (donor and acceptor) in close proximity *via* dipole–dipole interaction. High concentration of dopants is required in ETU process-dominated upconversion materials, as the dopant content determines the distance between the proximal ions. ETU can be classified into three categories based on diverse energy transfer types: successive energy transfer (SET), cross relaxation (CR) and cooperative upconversion (CU).

2.2.1 Successive energy transfer (SET). The SET process is illustrated in Fig. 3b. The donor ions in the excited state should match the energy requirement with proximal acceptor ions in the ground state. Consequently, the donor ions will transfer energy to the acceptor ions and excite them into the excited state (E_1), albeit themselves will return to the GS through non-radiative relaxation. The excited acceptor ions may be promoted to higher excited state (E_2) *via* successive energy transfer.

2.2.2 Cross relaxation (CR). The CR process between one or two types of neighboring ions is displayed in Fig. 3c. Both Ion_1 and Ion_2 (Ion_1) are populating the intermediate energy level (E_1 and E_2). Then, Ion_2 (Ion_1) would be motivated to higher intermediate energy level (E_3) in accordance with the non-radiatively energy transfer processes of proximal Ion_1, accompanied by the relaxation of Ion_1 to the ground state.

2.2.3 Cooperative upconversion (CU). Three ions are involved in the CU process (Fig. 3d), where the two excited ions (Ion_1 and Ion_2) transfer the energy to the third ion (Ion_3) simultaneously and emit Ion_3 from the GS to higher energy level, while Ion_1 and Ion_2 relax non-radiatively to the GS. The CU process involves the interaction between three ions, and the acceptor ions require a matched metastable energy level with donor ions; therefore, the CU process always occurs with low probability.[31]

2.3 Phonon avalanche (PA)

The PA process was proposed firstly from an investigation of the upconversion spectrum of Pr^{3+}-doped lanthanum chloride ($LaCl_3$) host by Chivian.[38] The PA process is an unconventional looping process of ESA and CR, which contains four procedures of energy transfer (Fig. 3e). (I) The Ion_2 initially emerges to the intermediate level (E_1) by GS energy transition. (II) This is followed by energy transfer by ESA or ETU process to populate the higher excited energy level (E_2) where the upconversion luminescence occurred. And then (III) a CR process occurred among activated Ion_2 and proximal ground-state Ion_1, causing two populations in the metastable state E_1. (IV) Finally, the looping process readily populates and exponentially increases the population of excited state E_2 through ESA process, invoking intense upconversion radiation like an avalanche process. The PA process is highly dependent on the pump intensity, which should be higher than the threshold value of metastable energy level.[39]

In addition, with the rapid development of core–shell nanostructured upconversion materials, a new energy migration-mediated upconversion (EMU) mechanism was proposed recently (Fig. 3f).[40,41] This involves successive energy transfer from the sensitizers (S) to accumulators (A′) and migrators (M), and trapped by activators (A), finally inducing the upconversion process.

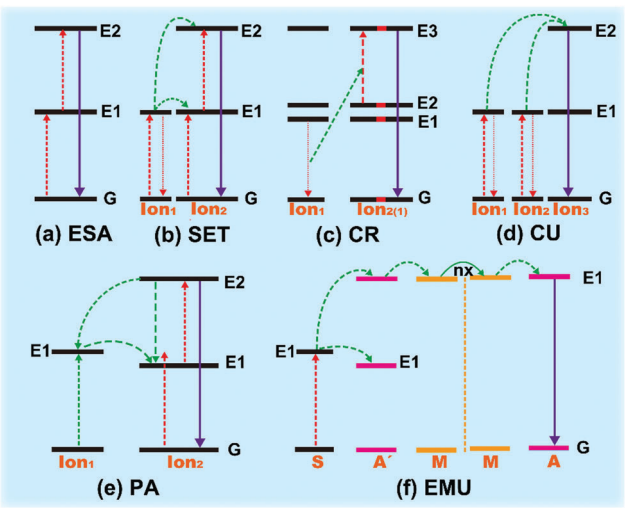

Fig. 3 Principal diagram for the upconversion processes of Ln^{3+}-doped crystals. (a) ESA, (b) SET, (c) CR, (d) CU, (e) PA and (f) EMU. The red, green, and purple lines stand for photon excitation, energy transfer, and emission processes, respectively.

3. The Ln^{3+} ion-doped upconversion materials

The upconversion efficiency of Ln^{3+} ion-doped materials is reliant on the crystal structures, local site symmetry, crystal

field strength, and phonon energy of the host matrixes. It will be a key factor to choose appropriate host matrixes to achieve favorable optical performance of upconversion materials with high upconversion luminescence efficiency. Currently, the majority of upconversion materials are doped with Ln^{3+} ions into appropriate dielectric host matrix. The doped Ln^{3+} ions are randomly distributed in the cation sites, which are offered by the ordered array of host matrixes.[42] The host matrixes generally do not constitute the exciting energy levels but will provide suitable crystal field for the doped Ln^{3+} ions that enables corresponding emissions. Host matrixes with low phonon energy are preferred for effective upconversion luminescence, because multi-phonon supported non-radiative relaxations between the nearest spaced energy levels can be minimized, thus greatly prolonging the lifetime of intermediate levels. The non-radiative relaxation probability (W_p) induced by multi-phonon relaxation is expressed as:[43,44]

$$W_p = C\left[\frac{\exp(hw/KT)}{\exp(hw/KT)^{-1}}\right]^{p} e^{-\alpha\Delta E} \quad (2)$$

where P is the order of phonons ($P = \Delta E/hw$), ΔE is the gap between two energy levels, w is the phonon frequency, h is the Boltzmann constant, and α and C are constants related to matrix materials. P will increase with decreasing phonon energy, resulting in the decrease of non-radiative relaxation possibility, thus enhancing the upconversion luminescence efficiency. Furthermore, the increased lifetime of metastable energy levels will prohibit the quenching of radiative transitions in the upconversion process. The phonon energy depends on the crystal lattice of host matrixes, and charge and diameter of anions implanted in the crystal. When the phonon energy matches the frequency of excitation or emission, the absorption of the crystal lattice can reduce the emission efficiency, and thus the host matrix is desirable to occupy with lower phonon energy. The most investigated host matrixes include low phonon energy (fluorides $\sim$355 cm^{-1}, chlorides $\sim$260 cm^{-1}, oxides $\sim$600 cm^{-1}, iodides $\sim$144 cm^{-1}, bromides $\sim$172 cm^{-1}, *etc.*) and high phonon energy (silicates $\sim$1000 cm^{-1}, borates $\sim$1100 cm^{-1}, phosphates, *etc.*) materials,[35,45–47] as listed in Table 1. Considering the effect of the photon energy of host matrixes on the upconversion luminescence, the efficiency increases in the order of oxides < fluorides < chlorides < bromides < iodides. Comparatively, heavy halides are hygroscopic, and the structural stability of the matrixes decreased in inversed proportional of oxides > fluorides > chlorides. Therefore, a series of investigations were carried out, expecting to find new-fashioned host matrixes with advantages of high upconversion efficiency (like fluorides and chlorides) and high stability (like oxides), to achieve practical applications. Typically, the hexagonal $NaYF_4$ crystal with low phonon energy and excellent chemical stability is accepted to be the most efficient host material hitherto.

In the following section, the effectiveness of commonly investigated upconversion materials with different host matrixes that are applied in the field of photocatalysis, including a sequence of $NaYF_4$-based, fluoride-based, oxide-based and Ln^{3+} ion-doped semiconductor-based photocatalysts, is discussed in detail.

Table 1 The phonon energy of various host matrixes

Host matrix	Phonon energy (cm^{-1})	Host matrix	Phonon energy (cm^{-1})
Fluorides	~355	Silicates	~1000
Chlorides	~260	Borates	~1100
Iodides	~144	Phosphates	~1300
Bromides	~172	Bismuthates	~1192
Oxides	~600		

4. The upconversion semiconductor-based photocatalysts

4.1 The mechanism of upconversion semiconductor-based photocatalysts

The proposed photocatalytic mechanism of semiconductor-based upconversion photocatalysts is illustrated in Fig. 4. The upconversion materials serve as the frequency conversion element and harvest two or multiple NIR light photons and then convert them into UV or visible light photons *via* an efficient fluorescent resonance energy transfer (FRET) process. Subsequently, the converted photons can be re-absorbed by the surrounding semiconductors and inject the electrons from VB to CB of semiconductors, thereby increasing the yield of photoinduced carriers. The direct energy migration between the combination of UC materials and semiconductors under NIR light irradiation could extend the utilization of the solar spectrum and promote the photocatalytic efficiency.

4.2 The $NaYF_4$-based upconversion photocatalysts

RE ion-doped sodium fluoride matrix contains two different types of crystal phases, including cubic and hexagonal phases (Fig. 5a and b). In the cubic phase, the host F^- ions form a high-symmetry cubic crystal structure, with Na^+ and RE^{3+} ions randomly occupying the cation sites. Comparatively, the Na^+ and RE^{3+} ions are selectively occupying the two types of relatively low-symmetry cation sites that are contained in regular crystal sublattices of F^- ions in hexagonal $NaYF_4$.[42]

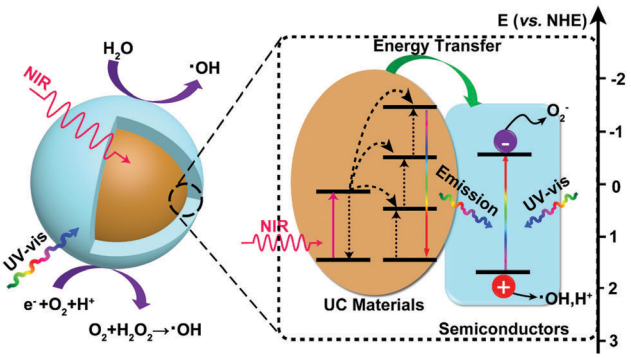

Fig. 4 The proposed photocatalytic enhancement mechanism for semiconductor-based upconversion photocatalysts.

Generally, host crystal lattices with low site symmetry of doping lanthanoids are preferable for upconversion luminescence over their higher symmetry counterparts, because low-symmetry lattices ordinarily have a crystal field with lots of uneven components surrounding the doping ions. The uneven components strengthen the electronic coupling among 4f electronic orbits and their higher electronic configuration and subsequently promote 4f–4f transition possibilities of the doping ions.[48] The density functional theory (DFT)-calculated charge densities for cubic and hexagonal $NaREF_4$ crystals are presented in Fig. 5c and d. In the hexagonal phase, the Ln^{3+} dopants increase the asymmetry distribution and improve the charge transfer, resulting in an enhancement of polarizability and formation energy. Therefore, hexagonal phase $NaREF_4$ nanocrystals exhibited an order of magnitude augmentation in upconversion efficiency when compared with cubic phase.[49] Especially, the hexagonal phase $NaYF_4$, having the advantages of wide energy bandgap ($\sim$8 eV)[50] and a very low phonon energy ($\sim$360 cm^{-1} $\approx$ 45 meV),[51,52] has been considered as one of the most efficient upconversion host matrixes for decades. And most photocatalysts have been combined with hexagonal phase $NaYF_4$ to achieve efficient NIR-active photocatalytic systems.

The photodegradation performance of $NaYF_4$-based semiconductor photocatalysts is presented in Table 2. As mentioned above, TiO_2 attracts extensive interest as a photocatalyst because the numerous advantages like abundance, chemical stability, environmental friendliness, and high photocatalytic activities. Incorporating upconversion materials with TiO_2 will extend the absorption edge up to the NIR region and finally achieve higher photocatalytic efficiency.[53–57] For example, core–shell $NaYF_4$:Yb,Tm@TiO_2 nanoparticles show excellent activities under both UV and NIR irradiation for photodegradation of RhB dyes.[55] And the photocatalytic activities of $NaYF_4$:Yb,Tm@TiO_2 nanoparticles vary with the sizes of the $NaYF_4$ core (Fig. 6a–d), the optimum core size being about 50 nm, which is beneficial to the photocatalytic performance of the TiO_2 shell. In addition, the size-dependent upconversion mechanism of $NaYF_4$:Yb^{3+},Er^{3+} nanoparticles has been experimentally and theoretically demonstrated, confirming the competition process between the upconversion population and non-radiative relaxation.[58] Another group further synthesized shell thickness-controllable $NaYF_4$@TiO_2 core–shell composites by varying the ratio of Yb^{3+},Tm^{3+} co-doped $NaYF_4$ microrods and Ti precursors (Fig. 6e–h), proving that optimum shell thickness is beneficial to the photocatalytic performance.[57] As displayed in Fig. 6i, when a thin TiO_2 shell is coated, only a small part of the UV radiation would be captured by the TiO_2 layer and most of it will be scattered and wasted. On the contrary, a thick TiO_2 shell will greatly inhibit the upconverted emissions penetrating to the external surface and largely increase the recombination possibilities of photogenerated carriers, which is also detrimental to photocatalytic performance. Furthermore, other upconversion material–semiconductor composite photocatalytic systems are rationally designed. For example, $NaYF_4$:Yb/Tm–BiOCl,[59] $NaYF_4$:Yb/Er–MoS_2,[60] $NaYF_4$:Yb/Tm–g-C_3N_4,[61,62] $NaYF_4$:Yb/Tm–CdS,[63,64] $NaYF_4$:Yb/Er–CdSe,[65] $NaYF_4$:Yb/Tm–ZnO,[66,67] and $NaYF_4$:Yb/Tm-MOFs[68] have been designed and constructed as NIR-responsive photocatalysts. Ternary heterogeneous materials are also developed and applied as highly efficient UV-visible-NIR full-spectra active photocatalysts.[69,70]

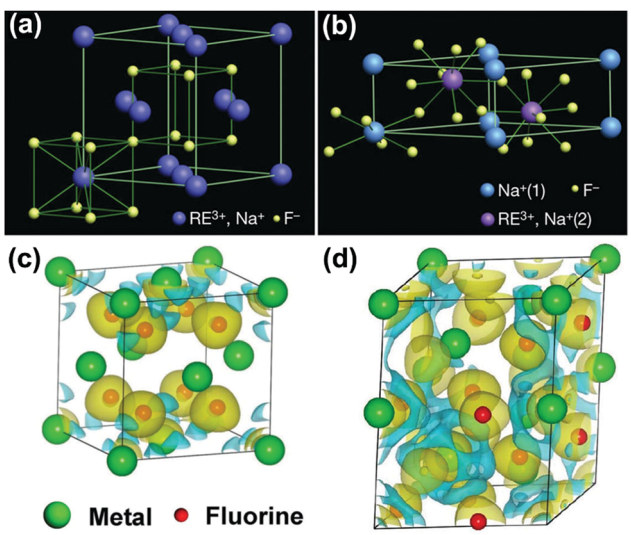

Fig. 5 (a) Cubic and (b) hexagonal type crystal phases of Ln^{3+}-doped $NaYF_4$ and DFT-calculated charge density for (c) cubic and (d) hexagonal $NaYF_4$. (Reproduced with permission.[42] Copyright 2010, Springer Nature.)

Unfortunately, upconversion nanomaterials always suffer the drawbacks of low quantum yields and intense luminescence quenching, mainly resulting from the comparatively insensitive extinction coefficients of lanthanide dopants.[27] Innovative methods have been investigated for enhancing the upconversion intensity in lanthanide-doped nanocrystals, including surface plasmon coupling, surface passivation, energy transfer modulation, *etc.*[27] Especially, the surface plasmon coupling of noble metals with upconversion material–semiconductor system presents fascinating NIR-driven photocatalytic performance.[71–74] Surface plasmon coupling of noble metals with upconversion materials improves the upconversion luminescence from three aspects as follows: (1) enhancing the absorption of the sensitizer through electric-field coupling, (2) improving the radiative decay rate of the activator, and (3) increasing energy transfer from the sensitizer to the activator, as displayed in Fig. 7a. The SPR-induced local electric field could enhance the photon flux and affect the radiative decay rates of the activators, thereby leading to enhanced upconversion luminescence and high quantum yield.[75,76] In our previous work, finite-difference time-domain analysis (FDTD) was used to stimulate the electromagnetic field intensity of upconversion and plasmonic enhanced photocatalysts under each of UV, visible and NIR light irradiation (Fig. 7b–e). The SPR effect of Ag nanoparticles leads to higher photocarrier yield and improves the efficient transfer of photocarriers and energy, resulting in quintupled enhancement of photocatalytic efficiency.[72] The plasmon and upconversion enhanced broadband photocatalysts NYF@TiO_2–Au are synthesized with significantly superior photocatalytic performance to the commercial P25 TiO_2.[71] Fig. 7f illustrates the NIR-active photocatalytic mechanism.

Table 2 Photodegradation performance of $NaYF_4$-based semiconductor photocatalysts

Photocatalyst (mg)	Light source	Pollutant[a] (concentration, mg L^{-1}/volume, mL)	Degradation ratio/time (h)	Ref.
$NaYF_4$:Yb/Tm@TiO_2 (0.5)	980 nm laser (10 W cm^{-2})	MB (15/0.5)	65%/14	53
$NaYF_4$:Yb/Tm@TiO_2 (20)	980 nm laser (0.5 A)	RhB (10^{-5} M/10)	22%/1 (83%/6)	54
	ARC lamp (69920)	Phenol (10^{-5} M/50)	17%/1 (53%/6)	
$NaYF_4$:Yb,Tm@TiO_2 (7)	50 W Xe lamp	RhB (5×10^{-5} M/50)	100%/0.5	55
$NaYF_4$:Yb/Tm@TiO_2	1 W 980 nm laser	MB (20/0.5)	68%/24	56
		MO (15/0.5)	69%/24	
		RhB (10/0.5)	76%/76	
$NaYF_4$:Yb/Tm@TiO_2 (10)	1.5 W 980 nm laser	MB (5/1)	90%/12	57
$NaYF_4$:Yb/Tm–BiOCl (20)	300 W Xe lamp, $\lambda > 780$ nm	RhB (10/50)	100%/2.7	59
		MB (10/50)	58%/2.7	
MoS_2–$NaYF_4$:Yb/Er (20)	980 nm laser	RhB (25/10)	61%/12	60
$NaYF_4$:Yb/Tm/g-C_3N_4 (1)	1 W 980 nm laser	MB (15/0.5)	83%/6	61
	300 W Xe lamp		89%/1.5	
$NaYF_4$:Yb/Tm/g-C_3N_4 (10)	1 W 980 nm laser	RhB (10/100)	22%/7	62
	50 W Xe lamp		80%/1.75	
$NaYF_4$:Yb/Tm–CdS (20)	2 W 976 nm laser	RhB (10/10)	13%/3	63
(40)	300 W Tu lamp	(50/20)	72%/2.5	
$NaYF_4$:Yb/Tm@C@CdS (10)	50 W Xe lamp	RhB (10^{-5} M/50)	92%/1.2	64
		MB (10^{-5} M/50)	95%/1.2	
$NaYF_4$:Yb/Er–CdSe (0.5)	2 W 1560 nm laser	MB (15/0.5)	65%/30	65
	2 W 980 nm laser		75%/30	
$NaYF_4$:Yb/Tm–ZnO (0.5)	2 W 980 nm laser	RhB (20/0.5)	65%/30	66
$NaYF_4$:Yb/Tm@SiO_2–ZnO (50)	980 nm laser (50 mW cm^{-2})	RhB (10/50)	17%/7	67
	50 W Xe lamp		89%/1.7	
$NaYF_4$:Yb/Tm/MOFs (20)	Xe lamp (100 mW cm^{-2})	RhB (10/50)	85%/1.5	68
$NaYF_4$:Yb/Tm@TiO_2/RGO (5)	2 W 980 nm laser	MB (10/5)	81.1%/12 (90%/1)	69
	300 W Xe lamp	MO (15/5)	45.9%/12 (90%/1)	
		Phenol (20/5)	29.8%/12 (61%/1)	
$NaYF_4$:Yb/Er@TiO_2–$Ag_6Si_2O_7$ (5)	2 W 980 nm laser	MB (10/10)	45%/5	70
	300 W Xe lamp		100%/2 min	
$NaYF_4$@TiO_2–Au (10)	8 W UV lamps	MO (20/100)	95%/1	71
	300 W Xe lamp ($\lambda > 420$ nm)		83%/8	
	2 W 980 nm laser		80%/20	
	150 W solar simulator		80%/2	
$NaYF_4$:Yb/Tm@SnO_2/Ag (5)	2 W 980 nm laser	RhB (10/10)	100%/5	72
	300 W Xe lamp		100%/0.17	
$NaYF_4$:Yb/Tm@TiO_2/Ag	50 W Xe lamp	R6G (10^{-5} M/50)	96%/2	73
$NaGdF_4$:Yb/Er–mTiO_2	AM 1.5 solar light	RhB	99%/0.8	77
$NaGdF_4$:Er/Yb@$BiFeO_3$ (20)	980 nm laser (80 mW mm^{-2})	MO (10/20)	55%/3.5	78
	500 W Xe lamp ($\lambda > 420$ nm)		80%/15	
$NaLuF_4$:Gd,Yb,Tm@SiO_2@TiO_2:Mo	500 W Xe lamp	RhB (20/50)	100%/3.5	79
	980 nm laser		90%/3.5	
$NaGdF_4$:Yb:Er/Ag/TiO_2 (8)	1.5 W 980 nm laser	RhB (5/5)	40%/18	80
(40)	500 W UV-vis light	(40/40)	97%/0.5	
$NaYF_4$:Yb/Tm@$NaYF_4$/TiO_2 (10)	8 W 980 nm laser	RhB (1.43/5)	41%/6	85
	250 W Xe lamp		73%/0.42	
$NaYF_4$:Tm/Yb@Yb/Nd@N–TiO_2	Xe lamp (100 mW cm^{-2})	RhB (10^{-5} M/50)	96%/1.5	86

[a] MB represents methylene blue; RhB represents Rhodamine B; MO represents methyl orange; R6G represents Rhodamine 6G.

Under NIR light irradiation, Er^{3+} and Tm^{3+} co-doped $NaYF_4$ excites UV and visible emissions, which overlap with the intrinsic light absorption of TiO_2 and SPR band of Au nanoparticles. The excited UV emissions will assist the TiO_2 to generate reductive electrons and highly oxidative holes. The excited visible emissions will interact with the SPR effect of Au nanoparticles to facilitate the transfer of hot electrons to nearby TiO_2 layer and minimize the electron–hole recombination. Finally, the broadband, effective nanohybrid photocatalyst improves the efficient electron and energy transfer among constituent components that leads to excellent photocatalytic activity. However, the direct contact of noble metal nanoparticles with upconversion materials is prejudicial to the fluorescence efficiency, because direct electron transfer or FRET occurs.[27] For boosting the fluorescence emissions, a minimum distance between them should be maintained of at least 5 nm, which is propitious for decreasing the non-radiative processes and increasing the radiative decay rate.[76]

Other Ln^{3+} ion-doped sodium fluoride-based phosphors such as $NaGdF_4$ and $NaLuF_4$ also have been investigated as promising frequency conversion candidates for NIR photocatalysts.[77–80] For example, β-$NaLuF_4$ and tetragonal-phase $LiLuF_4$ are reported as novel host matrixes that may show higher yields of upconversion efficiency than β-$NaYF_4$,[81–83] ascribed to the distinctive electronic states at the top valence band of Lu^{3+} ions and the smaller lattice-cell volume counterparts.

Besides, to construct core–shell structural upconversion nanocrystals through epitaxial growth of small lattice-mismatched

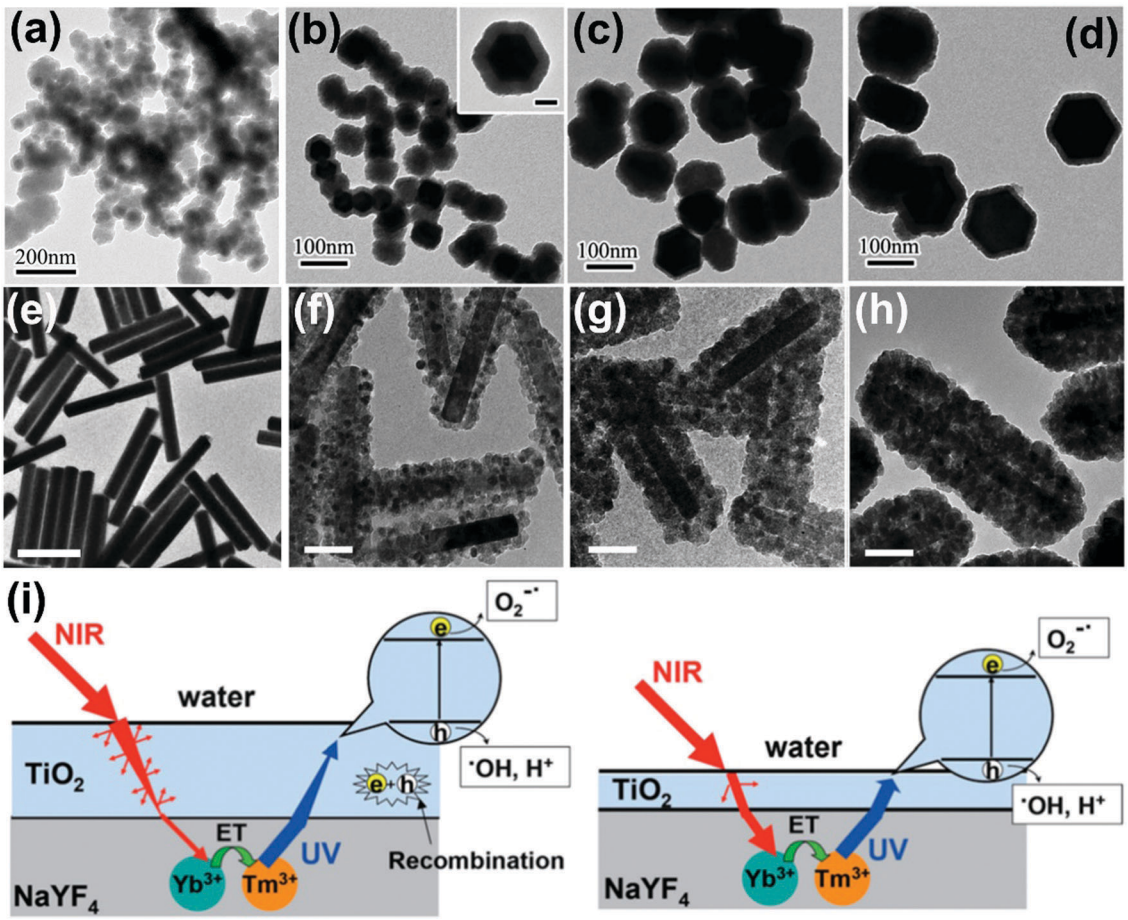

Fig. 6 TEM images of $NaYF_4$:Yb,Tm nanoplates of different sizes: (a) 30 nm, (b) 50 nm, (c) 100 nm, (d) 130 nm covered with amorphous TiO_2 shell. (Reproduced with permission.[55] Copyright 2014, Royal Society of Chemistry.) TEM images of (e) $NaYF_4$:Yb^{3+},Tm^{3+} microrods and (f–h) $NaYF_4$:Yb^{3+},Tm^{3+}@TiO_2 composites with different thickness of TiO_2 shell (scale bars: (e) 1 μm, (f–h) 100 nm). (Reproduced with permission.[57] Copyright 2013, Royal Society of Chemistry.) (i) The effect of various TiO_2 shells on photocatalytic mechanisms (left: thick shell; right: moderate shell). (Reproduced with permission.[57] Copyright 2013, Royal Society of Chemistry.)

layers is excepted as a fascinating approach for improving the upconversion features, by reducing the non-radiative decay losses. The outer layers would confine the doping ions in the interior core crystals and thus inhibit the surface energy loss, resulting in improved upconversion yields. For example, excellent upconversion efficiency improvements of about 7- and 79-fold were realized after epitaxial coating of $NaYF_4$ shell on the $NaYF_4$:Yb,Er(Tm) core, respectively.[84] Attributed to valid surface passivation, Huang *et al.* achieved record high upconversion quantum yield of 7.6% for $LiLuF_4$:Yb,Tm@$LiLuF_4$ core/shell upconversion nanoparticles.[81] Until now, there are only two studies applied to the core/shell structured $NaYF_4$:Yb/Tm@$NaYF_4$ and $NaYF_4$:Tm/Yb@Yb/Nd luminescent cores as energy transducers that combine with TiO_2 semiconductor for environmental purification.[85,86] Therefore, there are still bright prospects for development of core/shell upconversion nanoparticles for photocatalytic application.

4.3 The fluoride-based upconversion photocatalysts

Because of the closely arranged energy gaps of Ln^{3+} ions, host matrixes with low photonic energy are needed to overcome the non-radiative loss between the excited levels for realizing sensitive fluorescent transitions. Yttrium fluoride (YF_3) takes advantage of low vibration energy ($\sim$355 cm^{-1}) that could reduce the quenching of electron transitions within the 4f shell, and has been selected as an appropriate candidate for matrix materials.[25] A model of the orthorhombic YF_3 structure is displayed in Fig. 8a, where the Ln^{3+} ions will mainly occupy the interstitial sites of YF_3 crystals at low doping concentration and substitute the sites of Y^{3+} ions at high doping concentration.[87,88] Various trivalent lanthanide ion-doped YF_3 crystals with micro- and nanostructural morphologies (Fig. 8b–h) have been synthesized with hydrothermal process, reverse micelle method, thermal decomposition method, micro-emulsion method and microwave method by alternatively parameterizing the reaction conditions.[89–93] Additionally, the sizes, morphologies and phases could be manipulated for colorful emitting luminescence properties of Ln^{3+} ion-doped YF_3 nanocrystals which could act as frequency conversion elements for wide application in NIR-driven photocatalysis.

Also, Ln^{3+} ion-doped fluoride nanocrystals are coupled with conventional semiconductors to fabricate NIR-active photocatalysts.[94] For instance, peanut-like YF_3:Yb^{3+},Tm^{3+} nanocrystals

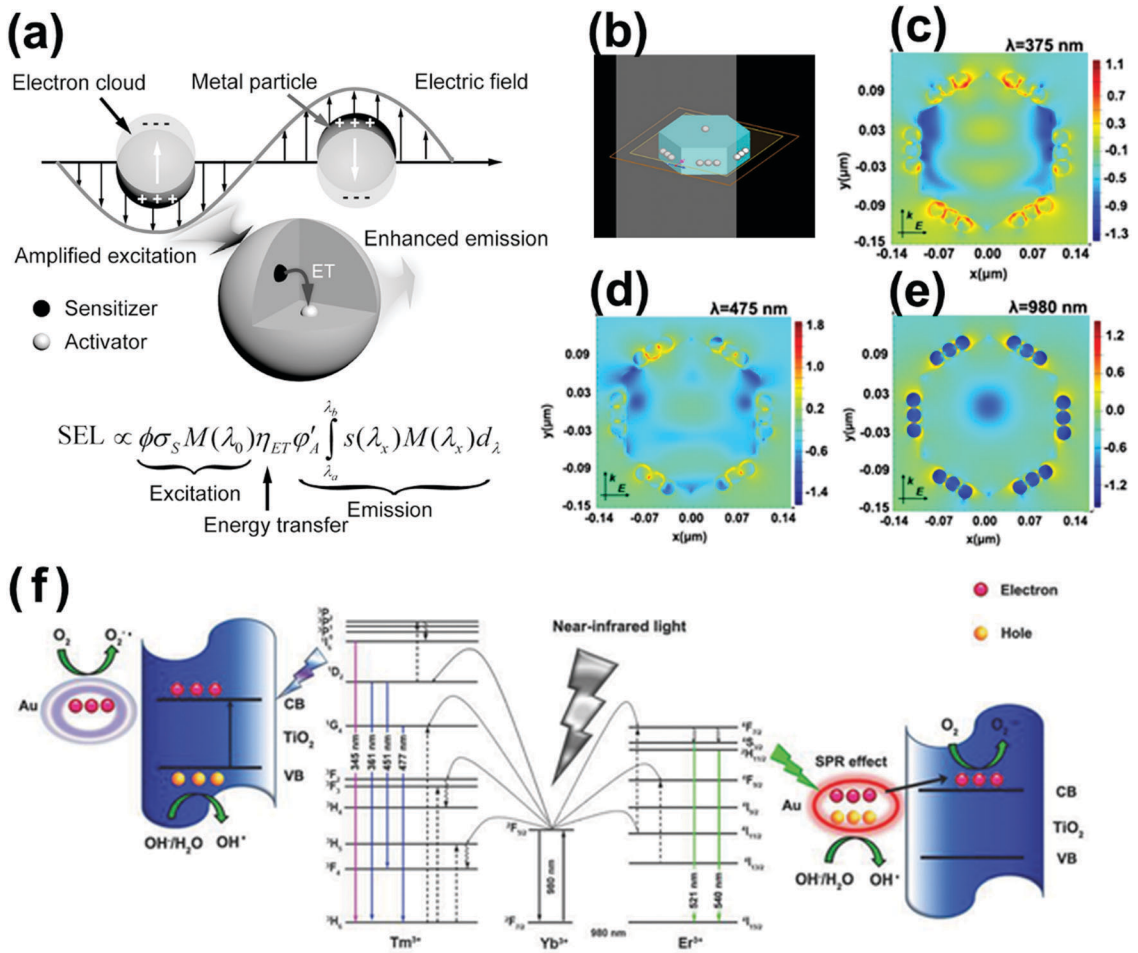

Fig. 7 (a) Plausible mechanism for plasmonic enhancement of upconversion emissions. (Reproduced with permission.[27] Copyright 2014, John Wiley and Sons.) (b–e) FDTD-calculated local electric field enhancement for $NaYF_4$@SnO_2@Ag nanoparticles at different incident wavelengths of 375, 475 and 980 nm. (Reproduced with permission.[72] Copyright 2017, American Chemical Society.) (f) Schematic photocatalytic mechanism of NYF@TiO_2–Au under NIR excitation. (Reproduced with permission.[71] Copyright 2015, John Wiley and Sons.)

with high specific surface were coated with uniform TiO_2 shell, expanding the light utilization threshold to the NIR region.[95] Bi^{3+} ions were further doped in YF_3 by substituting Y^{3+} ions to tailor the energy transfer process between Yb^{3+} with Er^{3+}/Tm^{3+}. The Bi^{3+} ions possessing larger ionic radius will increase the cell volume of matrixes and adjust the crystal field symmetry, therefore prolonging the lifetimes of the metastable energy states by changing their wave functions, and finally enhancing the upconversion emissions.[96,97] Additionally, the vacancies and point defects in Ln^{3+} ion-doped calcium fluoride (CaF_2) matrix will induce charge compensation effects, thus increasing the energy transfer rates and the upconversion probability.[98,99] The non-toxic, stable, abundant and nonhygroscopic features of CaF_2 have received increasing attention in fabrication of NIR-driven photocatalysts.[100–105] For example, by integrating Er^{3+}/Tm^{3+}/Yb^{3+} tri-doped CaF_2 nanocrystal with magnetic $ZnFe_2O_4$ and ZnO, a multi-component and multi-functional NIR photocatalyst, ETY-FCZ, was fabricated.[104] The ETY-FCZ presents continuous degradation of salicylic acid (SA) (Fig. 8i) and MO (Fig. 8j) with 71.9% and 43.73% removal rates when exposed to visible-NIR light irradiation for 180 min, respectively. Fig. 8k presents the proposed photocatalytic mechanism of the ETY-FCZ system, where the upconversion emitted UV-visible photons boosted the generation rates of electron–hole pairs of the ZnO–$ZnFe_2O_4$ heterostructures. Examples of fluoride-based upconversion photocatalysts based on the recent literature are presented in Table 3.

4.4 The RE sesquioxide-based upconversion photocatalysts

Although the phonon energy of RE sesquioxide materials (Y_2O_3, Gd_2O_3, Lu_2O_3, La_2O_3, *etc.*) is high, their excellent chemical/thermal stability makes them promising luminescence matrix candidates. Y_2O_3 is regarded as the best sesquioxide matrix for lanthanoids with smallest phonon energy ($\sim$380 cm^{-1}) among other metallic oxides and similar ionic radius (90 pm) to lanthanide elements. The ionic radii of Ln^{3+} are listed in Table 4, where the ionic radii (assuming six-coordination) reduce from 106.1 pm for La^{3+} ions to 84.8 pm for Lu^{3+} ions accompanied with an increase of atomic number. The similar ionic radii of Ln^{3+} ions to host cations will hinder the

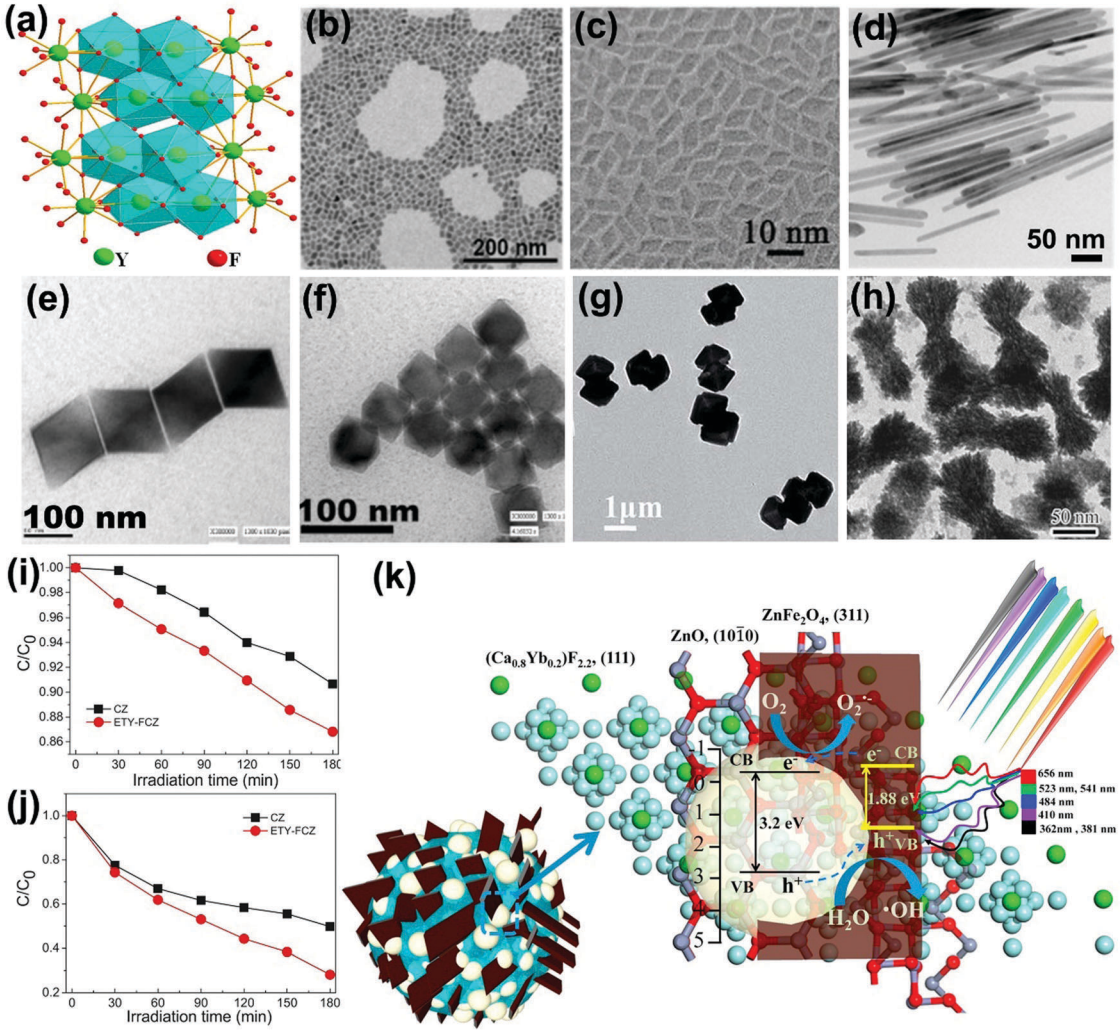

Fig. 8 (a) Schematic representation of orthorhombic structure. (Reproduced with permission.[87] Copyright 2017, American Chemical Society.) Typical YF_3 morphologies of (b) nanospheres (reproduced with permission;[88] copyright 2014, Royal Society of Chemistry), (c) rhombic shapes (reproduced with permission;[89] copyright 2014, Royal Society of Chemistry), (d) nanorods (reproduced with permission;[91] copyright 2017, American Chemical Society), (e) quadrilateral-shaped particles (reproduced with permission;[90] copyright 2005, American Chemical Society), (f) hexagonal particles (reproduced with permission;[90] copyright 2005, American Chemical Society), (g) dumbbell-shaped particles (reproduced with permission;[92] copyright 2017, Royal Society of Chemistry) and (h) peanut-like nanocrystals (reproduced with permission;[95] copyright 2013, Elsevier BV). The photocatalytic performances of as-fabricated NIR-driven photocatalyst ETY-FCZ for degradation of (i) SA and (j) MO, and (k) the proposed photocatalytic mechanism (reproduced with permission;[104] copyright 2015, Elsevier BV).

generation of crystal defects and lattice stress, and thus facilitating the upconversion efficiency.[106] More importantly, the distance of interacting ions (D) dominates the electric dipole–dipole energy transfer efficiency (P) between sensitizer and activator ions, which follows the relationship:[107]

$$P \sim \frac{1}{D^6} \quad (3)$$

where the nearest interaction distances of RE ions confined in the host lattice of Y_2O_3, Gd_2O_3, Lu_2O_3 and La_2O_3 are presented in Table 5. Comparatively, it can be predicted that a more efficient energy transfer could be achieved with the same lanthanide dopants in the Lu_2O_3 host than in the Gd_2O_3 and La_2O_3 hosts, and their upconversion efficiency may obey the sequence of $Lu_2O_3 > Gd_2O_3 > La_2O_3$. As mentioned above, the low vibration energy of Y_2O_3 matrix improves the probability of radiative transitions among electronic energy levels of lanthanide dopants, inducing the highest interacting energy transfer rate in sesquioxides.

Schematic illustrations of RE sesquioxide unit cells modeled according to the structural parameters in Table 5 are shown in Fig. 9.[108–110] The nanocrystalline systems of RE_2O_3 (RE = Y, Gd, Lu) prefer the formation of cubic structure with space group of *Ia*3 (No. 206) (Fig. 9a and b), while La_2O_3 is predisposed to unconventional hexagonal phase with space group of *P*3*m*1 (No. 164) (Fig. 9c and d). Theoretically, the polymorphism of RE sesquioxides with lighter atoms (La–Sm) generally means that they adopt the hexagonal structure and the heavier atoms

Table 3 Photodegradation performances of fluoride-based semiconductor photocatalysts

Photocatalyst (mg)	Light source	Pollutants (concentration, mg L^{-1}/volume, mL)	Degradation ratio/time (min)	Ref.
YF_3:Yb,Tm/TiO_2 (0.5)	1.5 W 980 nm laser	MB (15/0.5)	70%/1800	94
YF_3:Yb,Tm@TiO_2 (20)	50 W Xe lamp	MO (50/20)	85%/70	95
$NaY(WO_4)_2$/TiO_2/YF_3:Yb,Tm (20)	1000 W mercury lamp	MO (10/20)	100%/60	96
		SA (10/20)	90%/60	
CaF_2:Er,Yb@TiO_2 (50)	500 W Xe lamp (720 nm $< \lambda <$ 1 100 nm)	MB (10/50)	60%/720	100
		MO (10/50)	32%/720	
$BiVO_4$/CaF_2:Er,Tm,Yb (0.5)	980 nm laser (10 W cm^{-2})	MB (15/0.5)	75%/420	101
$CaWO_4$@(TiO_2/CaF_2:Er/Tm/Yb) (20)	980 nm laser (2 A)	MO (10/20)	20.29%/180	102
	1000 W mercury lamp ($\lambda \geq$ 780 nm)		46.57%/180	
$CaWO_4$@(TiO_2/CaF_2:Er/Tm/Yb) (20)	980 nm laser (2 A)	MO (10/20)	20.29%/180	103
	1000 W mercury lamp		99.02%/60	
CaF_2:Er/Tm/Yb@$ZnFe_2O_4$/ZnO (20)	1000 W mercury lamp ($\lambda \geq$ 400 nm)	MO (10/20)	71.9%/180	104
		SA (10/20)	43.73%/180	
CaF_2:Yb@$BiVO_4$ (20)	980 nm laser (2 A)	MO (10/10)	10%/360	105
	1000 W mercury lamp		41%/180	

Table 4 The ionic radii of Ln^{3+}

Element	La	Ce	Pr	Nd	Pm	Sm	Eu	Gd
Atomic number	57	58	59	60	61	62	63	64
Ionic radius[a] (10^{-12} m, pm)	106.1	103.4	101.3	99.5	97.9	96.4	94.7	93.8
Element	Tb	Dy	Ho	Er	Tm	Yb	Lu	—
Atomic number	65	66	67	68	69	70	71	—
Ionic radius (10^{-12} m, pm)	92.3	91.2	90.1	88.1	86.9	85.8	84.8	—

[a] Assuming six-coordination.

(Ho–Lu) prefer the cubic, whereas the intermediate atoms (Sm–Dy) can be stabilized in both cubic and monoclinic structures (Fig. 9e).[108] The lighter Ln^{3+} ions with larger ionic radii prefer the formation of hexagonal crystals in virtue of higher electron cloud distortion induced by increased dipole polarizability.[42] The results will offer us reasonable guidance for accommodating appropriate Ln^{3+} dopants in morphological construction engineering.

RE sesquioxide nanocrystals incorporated with semiconductors were employed for synthesis of photocatalysts for environmental cleaning and energy conversion.[111–116] For example, the Yb^{3+},Tm^{3+} co-doped Y_2O_3 upconversion luminescence agent was composited with TiO_2 and showed higher infrared-to-UV photocatalytic activity than non-doped TiO_2 under irradiation of solar light.[114] Another chain-like Er/Tm/Yb/Y_2O_3 composite demonstrated higher upconversion luminescent intensity than flake-like Er/Tm/Yb/Y_2O_3 upconversion nanoparticles, leading to better photocatalytic performance for degradation of MB dyes when coupling with 3C-SiC nanocrystals.[113] Furthermore, the Gd^{3+} ions with magnetic properties are used to fabricate optically and magnetically active bifunctional materials for advanced multifunctional photocatalysts.[112,117]

4.5 The Ln^{3+} ion-doped upconversion photocatalysts

In recent years, the doping of ions into a semiconductor matrix, including non-metal ions (P^{3-}, S^{2-}, Cl^{-}, *etc.*) and metal ions (Zn^{2+}, Cu^{2+}, Fe^{3+}, *etc.*), has become popular and a prime motivation to extend the optical absorption threshold, or trap the photogenerated electrons by induced oxygen vacancy and/or surface defect, finally improving the photoactivities.[4,9,118,119] Similarly, the current strategies of doping with Ln^{3+} ions into semiconductors such as TiO_2, ZnO, $BiVO_4$, *etc.*, have proved to be an interesting and not yet fully explored highway for optimizing the photocatalytic performance.[120–128] As displayed in Fig. 10, 4f orbital electronic states of Ln^{3+} ions bring the sub-bandgap levels that settled down below the conduction band edge of semiconductors. The electrons will populate the inserted electronic states of Ln^{3+} ions instead of intrinsic conduction

Table 5 Structural parameters of RE_2O_3 (RE: Y, La, Gd, Lu) nanocrystals

Hosts	Y_2O_3	Gd_2O_3	Lu_2O_3	La_2O_3
Phonon energy (cm^{-1})	~380	~600	~618	~400
Bandgap (eV)	5.6	5.4	6	5.5
Ionic radius[a] (10^{-12} m, pm)	90	93.8	84.8	106.1
Crystal system	Cubic	Cubic	Cubic	Hexagonal
Space group	$Ia\bar{3}$ (206)	$Ia\bar{3}$ (206)	$Ia\bar{3}$ (206)	$P\bar{3}m1$ (164)
Lattice parameters	$a = b = c$ = 10.6073 Å	$a = b = c$ = 10.8012 Å	$a = b = c$ = 10.3946 Å	$a = b$ = 3.9198 Å
				c = 6.1139 Å
	$\alpha = \beta = \gamma = 90^\circ$	$\alpha = \beta = \gamma = 90^\circ$	$\alpha = \beta = \gamma = 90^\circ$	$\alpha = \beta = 90^\circ$, $\gamma = 120^\circ$
Nearest RE distance (Å)	3.52 (Y1–Y2)	3.59 (Gd1–Gd2)	3.44 (Lu1–Lu2)	3.83 (La–La)
	3.53 (Y2–Y2)	3.61 (Gd2–Gd2)	3.46 (Lu2–Lu2)	

[a] Assuming six-coordination.

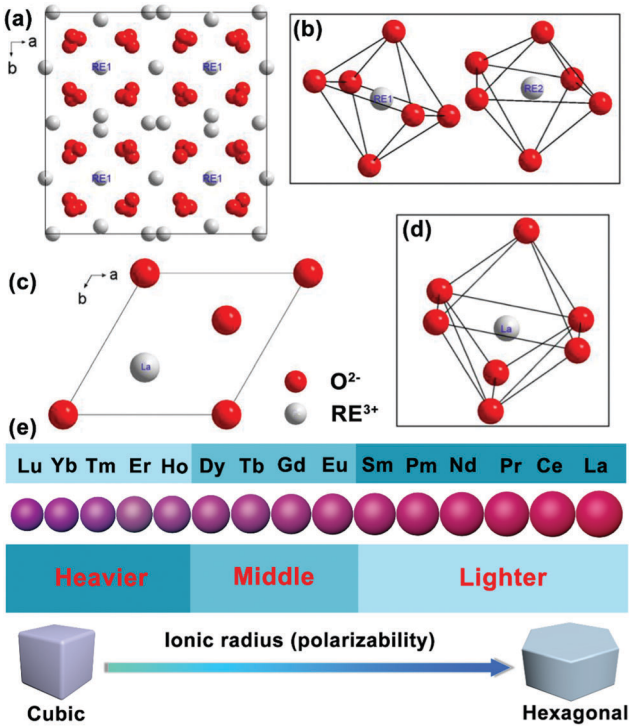

Fig. 9 Schematic illustration of the unit cell projected on *a*–*b* plane and the RE coordination polyhedra: (a and b) RE_2O_3 (RE = Y, Gd, Lu), (c and d) La_2O_3 (reproduced with permission;[108] copyright 2018, Elsevier BV). (e) Ionic radius (or polarizability) induced phase transition from cubic to hexagonal of Ln^{3+} ion-doped upconversion crystals.

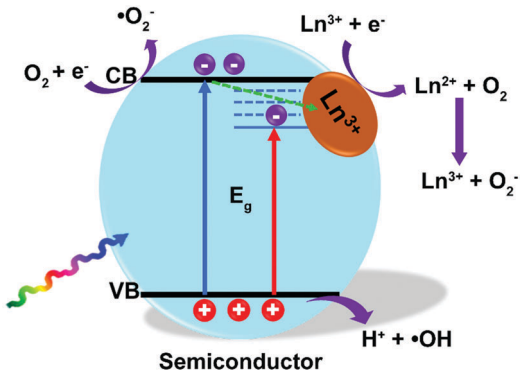

Fig. 10 Photocatalytic mechanism of Ln^{3+}-doped semiconductor photocatalysts.

band edge of semiconductors, thus narrowing the bandgap energy of photocatalysts and extending the optical absorption threshold.[129,130] For example, the bandgap energy values of B-$BiVO_4$ with different doping concentrations of Eu^{3+} ions varied from 0 to 1.0% were calculated by using the Kubelka–Munk function. The bandgaps were tailored from 2.36 eV to 2.26 eV by raising the dopant dosage of Eu^{3+} ions, inducing approximately nine times higher photocatalytic activity (0.8 Eu–B-$BiVO_4$) compared with pure $BiVO_4$.[131]

Additionally, the lanthanides are well known for being capable of forming complexes with a variety of Lewis bases, like amines, aldehydes, alcohols, and thiols, taking advantage of their functional groups and the f-orbitals of the lanthanoids.[34,132] Meanwhile, the substitution of high valence state ions (such as Ti^{4+}) with trivalent Ln^{3+} ions will break the charge balance, which may be compensated by negative functional groups of dyes.[133] This is desirable to increase the adsorption capacity of organic dyes with photocatalysts due to the negative functional group, therefore lying good preparatory foundations for subsequent photocatalytic reactions.[134] For example, three-fold higher adsorption constants k were achieved in Pr^{3+}/Eu^{3+} ion-doped TiO_2 photocatalysts that were analyzed according to Langmuir's theory.[135] The Ln^{3+} sites can act as electron acceptors to trap the photogenerated electrons and minimize undesired electron–hole recombination, where the trapped electrons are capable of combining with oxygen to form superoxide radicals for photooxidation of adsorbed organics. Especially, for Gd^{3+} ions with special half-filled electronic configuration of 7f-electrons, it is easier to transfer the trapped electrons to the interfacial adsorbed oxygen.[130,136]

It is well known that doping of Ln^{3+} ions will improve the photocatalytic performance of semiconductors by regulating the band energy and promoting the separation of carriers. Meanwhile, the loading concentration and type of Ln^{3+} dopant ions are also important parameters that affect the photocatalytic performance. High dopant dosage will increase the surface barrier of the semiconductors and decrease the space charge region. A large electric field is beneficial for promoting the separation of photoinduced carriers. But if the doping concentration is too high, the space charge region will become narrow that substantially reduces the penetration depth of light into semiconductors, and hence greatly increases the recombination possibilities of photoinduced carriers.[130,137] Moreover, owing to the generally large ionic radii of Ln^{3+} ions (Table 4), for example, larger than Ti^{4+} (~68 pm), small and isolated clusters of lanthanide oxide will form and cover the surface of semiconductors at high doping concentration, which will aggregate as carrier capture centers, thus deactivating the photocatalytic activity.[138] Therefore, there must be an optimum concentration level of dopants to balance the thickness of the space charge layer substantially equivalent to the light penetration depth. For instance, La^{3+} ion-doped TiO_2 at a concentration of 0.5% was proved to possess the most efficient photodegradation rate for MO counterparts.[139] And Dy^{3+}-doped ZnO nanoparticles with a doping concentration of 3% were found to endow the highest decolorization efficiency of C. I. Acid Red 17 under visible light irradiation.[140]

In the activator ion (*i.e.*, Tm^{3+}, Er^{3+}) and sensitizer ion (*i.e.*, Yb^{3+}, Nd^{3+}) co-doped semiconductor system, the sensitizer will accept the NIR photons and transfer the energy to the nearest activator ions for emitting UV-visible photons by the upconversion process. As mentioned above, the upconverted photons favor the donation to the valence band of semiconductor followed by oxidative hole (h^+) generation by extraction of a reductive electron, thus boosting the yield of photocarriers and improving the photocatalytic efficiency.[141,142]

5. Outlooks and perspectives

In summary, the synthesis of upconversion materials with effective quantum yields and fabrication of upconversion-based semiconductor photocatalysts are considerable challenges. Despite the significant developments in this direction, there are several tough challenges associated with upconversion materials that limit their applications in basic sciences, including lower upconversion yields and confined excitation wavelengths. However, the reported highest upconversion efficiency is 3.0 ± 0.3% for Yb^{3+},Er^{3+} co-doped bulk $NaYF_4$ materials.[143] Nevertheless, the micro- or nanomaterials possess lower upconversion efficiency than bulk materials because of the synergistic effect of surface state defects induced by the small particle sizes and adhering water reducing the optical efficiency. Therefore, much effort is required to design and develop high-efficiency upconversion materials. To achieve this purpose, the first method is to select host materials with low phonon energy, which prefer to decrease multi-phonon relaxation between closely spaced energy levels, thus generating more effective upconversion. The host materials provide a surrounding crystalline field for Ln^{3+} ions but do not determine the emissions. The type of lanthanide dopant and doping concentration are vital for tailoring the upconverted luminescence. In addition, the SPR effect of noble metals is proved theoretically and experimentally to boost the upconversion luminescence by enhancing the absorption of the sensitizer through electric-field coupling, improving the radiative decay rate of the activator, and increasing energy transfer from the sensitizer to the activator. The intrinsic features of SPR are greatly beneficial to the photocatalytic performance of semiconductor photocatalysts by boosting the yield of photogenerated electron/hole pairs and promoting their effective separation. In addition, the SPR of noble metal nanoparticles could effectively promote the efficiency of upconversion materials. Interestingly, researchers have recently discovered localized surface plasmon resonances (LSPRs) in heavily doped semiconductor nanoparticles, quantum dots and amorphous two-dimensional nanomaterials.[144–146] The occurrence of LSPR originates from collective oscillations of excess free carriers, the concentration of which (10^{19}–10^{21} cm^{-3}) can be regulated by adjusting stoichiometric ratios, vacancy or doping concentrations, phase structures, *etc.*[147] Therefore, the LSPR-induced electric field in semiconductors provides a powerful strategy to enhance the upconversion efficiency. More importantly, the unique interactions based on the process of plasmonic energy transfer will further improve the NIR light-active photocatalytic performance.[148,149] The marriage of upconversion with semiconductor LSPR could be a novel frontier in fundamental investigations and practical solar energy conversion applications.

Also, epitaxial growth of a shell with small lattice mismatch around a core can reduce non-radiative decay losses of the surface fluorescence, which would offer a useful way to improve the fluorescence intensity of upconversion crystals. In a core–shell structure, the dopant RE ions are incorporated into the interior core layer of particles. The shell layer can effectively suppress energy loss on the crystal surface, resulting in higher luminescence efficiency. These attractive features of core–shell structures make them suitable candidates for photocatalytic application.

The preceding discussion is concentrated entirely on Yb^{3+} ion (absorption cross section $\approx 10^{-20}$ cm^2)-sensitized upconversion materials with the photo-absorption band centered at 980 nm. By paying attention to the drawbacks of confined excitation wavelength, innovative strategies that incorporate replaceable sensitizers have been proposed for tuning the excitation wavelengths of upconversion crystals. Nd^{3+} is ideal as an alternative sensitizer since it has a one order of magnitude larger absorption cross section ($\approx 10^{-19}$ cm^2) at ≈800 nm than Yb^{3+} at ≈980 nm.[27] Benefiting from the unique features of deep tissue penetration depth and low photothermal effect of ≈800 nm light (first NIR window), the Nd^{3+}-sensitized upconversion nanoparticles have attracted considerable interdisciplinary attention in biosensing, bioimaging, drug delivery, therapy, and three-dimensional displays.[150] Unfortunately, there is no literature focusing on the Nd^{3+}-sensitized upconversion materials as energy conversion elements that are composited with semiconductor photocatalysts, for further utilizing solar light centered at 800 nm. The emergence of Nd^{3+}-sensitized upconversion nanoparticles would open other possible avenues of future works on upconversion semiconductor-based photocatalytic systems. We anticipate new breakthroughs in the construction of novel and highly efficient NIR-light-activated photocatalysts.

At present, almost all the considered NIR light-active photocatalytic systems are applied in organic dye degradation. It will be of significant importance to exploit potential effective photocatalysts for solving the challenges faced by the community of upconversion-based materials for their more efficient and wider applications to energy production and storage such as water splitting, CO_2 conversion, *etc.*[151,152]

Author contributions

All authors contributed during the preparation of the manuscript. All authors have given approval to the final version of the manuscript.

Conflicts of interest

The authors declare that they have no competing interests.

Acknowledgements

This work was supported by the NSFC (51471121), Hubei Provincial Natural Science Foundation (2014CFB261), Basic Research Plan Program of Shenzhen City (JCYJ20160517104459444), Natural Science Foundation of Jiangsu Province (BK20160383) and Wuhan University.

References

1 H. Tong, S. Ouyang, Y. Bi, N. Umezawa, M. Oshikiri and J. Ye, *Adv. Mater.*, 2012, **24**, 229–251.
2 W. Wu, J. Changzhong and V. A. Roy, *Nanoscale*, 2015, **7**, 38–58.
3 Z. Wu, S. Yang and W. Wu, *Nanoscale*, 2016, **8**, 1237–1259.
4 J. Liu, Z. Wu, Q. Tian, W. Wu and X. Xiao, *CrystEngComm*, 2016, **18**, 6303–6326.
5 C. Chen, W. Ma and J. Zhao, *Chem. Soc. Rev.*, 2010, **39**, 4206–4219.
6 L. Sun, W. Wu, S. Yang, J. Zhou, M. Hong, X. Xiao, F. Ren and C. Jiang, *ACS Appl. Mater. Interfaces*, 2014, **6**, 1113–1124.
7 Q. Tian, W. Wu, L. Sun, S. Yang, M. Lei, J. Zhou, Y. Liu, X. Xiao, F. Ren, C. Jiang and V. A. L. Roy, *ACS Appl. Mater. Interfaces*, 2014, **6**, 13088–13097.
8 W. Wu, S. Zhang, X. Xiao, J. Zhou, F. Ren, L. Sun and C. Jiang, *ACS Appl. Mater. Interfaces*, 2012, **4**, 3602–3609.
9 J. Liu, S. Yang, W. Wu, Q. Tian, S. Cui, Z. Dai, F. Ren, X. Xiao and C. Jiang, *ACS Sustainable Chem. Eng.*, 2015, **3**, 2975–2984.
10 A. Fujishima and K. Honda, *Nature*, 1972, **238**, 37–38.
11 J. H. Carey, J. Lawrence and H. M. Tosine, *Bull. Environ. Contam. Toxicol.*, 1976, **16**, 697–701.
12 B. Kraeutler and A. J. Bard, *J. Am. Chem. Soc.*, 1978, **100**, 5985–5992.
13 G. L. Amy, L. Linsebigler and J. T. Yates, Jr., *Chem. Rev.*, 1995, **95**, 735–758.
14 S. G. Kumar and L. G. Devi, *J. Phys. Chem. A*, 2011, **115**, 13211–13241.
15 H. Park, Y. Park, W. Kim and W. Choi, *J. Photochem. Photobiol., C*, 2013, **15**, 1–20.
16 Q. Tian, W. Wu, J. Liu, Z. Wu, W. Yao, J. Ding and C. Jiang, *Dalton Trans.*, 2017, **46**, 2770–2777.
17 W. Wu, L. Sun, S. Yang, J. Zhou, M. Hong, X. Xiao, F. Ren and C. Jiang, *ACS Appl. Mater. Interfaces*, 2014, **6**, 1113–1124.
18 H. Li, Z. Kang, Y. Liu and S.-T. Lee, *J. Mater. Chem.*, 2012, **22**, 24230–24253.
19 H. Li, R. Liu, S. Lian, Y. Liu, H. Huang and Z. Kang, *Nanoscale*, 2013, **5**, 3289–3297.
20 J. Wu, Z. Zhang, B. Liu, Y. Fang, L. Wang and B. Dong, *Sol. RRL*, 2018, **2**, 1800039.
21 M. Hu, J. Chen, Z.-Y. Li, L. Au, G. V. Hartland, X. Li, M. Marquez and Y. Xia, *Chem. Soc. Rev.*, 2006, **35**, 1084–1094.
22 A. Kubacka, M. Fernandez-Garcia and G. Colon, *Chem. Rev.*, 2012, **112**, 1555–1614.
23 Z. Zhang and J. T. Yates, Jr., *Chem. Rev.*, 2012, **112**, 5520–5551.
24 W. Yang, X. Li, D. Chi, H. Zhang and X. Liu, *Nanotechnology*, 2014, **25**, 482001.
25 X. Liu, H. Chu, J. Li, L. Niu, C. Li, H. Li, L. Pan and C. Q. Sun, *Catal. Sci. Technol.*, 2015, **5**, 4727–4740.
26 X. Li, F. Zhang and D. Zhao, *Chem. Soc. Rev.*, 2015, **44**, 1346–1378.
27 S. Han, R. Deng, X. Xie and X. Liu, *Angew. Chem., Int. Ed.*, 2014, **53**, 11702–11715.
28 S. Gai, C. Li, P. Yang and J. Lin, *Chem. Rev.*, 2014, **114**, 2343–2389.
29 X. Yu, M. Li, M. Xie, L. Chen, Y. Li and Q. Wang, *Nano Res.*, 2010, **3**, 51–60.
30 X. Yu, L. Chen, M. Li, M. Xie, L. Zhou, Y. Li and Q. Wang, *Adv. Mater.*, 2008, **20**, 4118–4123.
31 S. V. Eliseeva and J. C. Bunzli, *Chem. Soc. Rev.*, 2010, **39**, 189–227.
32 F. Wang and X. Liu, *J. Am. Chem. Soc.*, 2008, **130**, 5642–5643.
33 A. Shalav, B. S. Richards and M. A. Green, *Sol. Energy Mater. Sol. Cells*, 2007, **91**, 829–842.
34 S. Bingham and W. A. Daoud, *J. Mater. Chem.*, 2011, **21**, 2041–2050.
35 D. Chen, Y. Wang and M. Hong, *Nano Energy*, 2012, **1**, 73–90.
36 N. Bloembergen, *Phys. Rev. Lett.*, 1959, **2**, 84–85.
37 X. Li, F. Zhang and D. Zhao, *Nano Today*, 2013, **8**, 643–676.
38 J. S. Chivian, W. E. Case and D. D. Eden, *Appl. Phys. Lett.*, 1979, **35**, 124–125.
39 G. Chen, H. Qiu, P. N. Prasad and X. Chen, *Chem. Rev.*, 2014, **114**, 5161–5214.
40 F. Wang, R. Deng, J. Wang, Q. Wang, Y. Han, H. Zhu, X. Chen and X. Liu, *Nat. Mater.*, 2011, **10**, 968–973.
41 Q. Su, S. Han, X. Xie, H. Zhu, H. Chen, C.-K. Chen, R.-S. Liu, X. Chen, F. Wang and X. Liu, *J. Am. Chem. Soc.*, 2012, **134**, 20849–20857.
42 F. Wang, Y. Han, C. S. Lim, Y. Lu, J. Wang, J. Xu, H. Chen, C. Zhang, M. Hong and X. Liu, *Nature*, 2010, **463**, 1061–1065.
43 K. K. Pukhov, F. Pelle and J. Heber, *Mol. Phys.*, 2003, **101**, 1001–1006.
44 C. B. Layne, W. H. Lowdermilk and M. J. Weber, *Phys. Rev. B: Solid State*, 1977, **16**, 10–20.
45 X. Liu, M. Li, X. Wang, F. Huang, Y. Ma, J. Zhang, L. Hu and D. Chen, *J. Lumin.*, 2014, **150**, 40–45.
46 O. Ravi, S. J. Dhoble, B. Ramesh, G. Devarajulu, C. M. Reddy, K. Linganna, G. R. Reddy and B. D. P. Raju, *J. Lumin.*, 2015, **164**, 154–159.
47 Y. Jia, T.-Y. Sun, J.-H. Wang, H. Huang, P. Li, X.-F. Yu and P. K. Chu, *CrystEngComm*, 2014, **16**, 6141–6148.
48 W. Zheng, P. Huang, D. Tu, E. Ma, H. Zhu and X. Chen, *Chem. Soc. Rev.*, 2015, **44**, 1379–1415.
49 G. S. Yi and G. M. Chow, *Adv. Funct. Mater.*, 2006, **16**, 2324–2329.
50 K. Chong, T. Hirai, T. Kawai, S. Hashimoto and N. Ohno, *J. Lumin.*, 2007, **122–123**, 149–151.
51 C. Li, Z. Quan, J. Yang, P. Yang and J. Lin, *Inorg. Chem.*, 2007, **46**, 6329–6337.
52 M. Haase and H. Schäfer, *Angew. Chem., Int. Ed.*, 2011, **50**, 5808–5829.
53 Y. Tang, W. Di, X. Zhai, R. Yang and W. Qin, *ACS Catal.*, 2013, **3**, 405–412.
54 W. Wang, M. Ding, C. Lu, Y. Ni and Z. Xu, *Appl. Catal., B*, 2014, **144**, 379–385.
55 W. Su, M. Zheng, L. Li, K. Wang, R. Qiao, Y. Zhong, Y. Hu and Z. Li, *J. Mater. Chem. A*, 2014, **2**, 13486–13491.

56 D.-X. Xu, Z.-W. Lian, M.-L. Fu, B. Yuan, J.-W. Shi and H.-J. Cui, *Appl. Catal., B*, 2013, **142–143**, 377–386.
57 Y. Zhang and Z. Hong, *Nanoscale*, 2013, **5**, 8930–8933.
58 X. Chen, Y. Zhu, D. Zhou, W. Xu, J. Zhu, G. Pan, Z. Yin, H. Wang, S. Cui and H. Song, *J. Mater. Chem. C*, 2017, **5**, 2451–2458.
59 L. Bai, W. Jiang, C. Gao, S. Zhong, L. Zhao, Z. Li and S. Bai, *Nanoscale*, 2016, **8**, 19014–19024.
60 M. Chatti, V. N. Adusumalli, S. Ganguli and V. Mahalingam, *Dalton Trans.*, 2016, **45**, 12384–12392.
61 M. Z. Huang, B. Yuan, L. Dai and M. L. Fu, *J. Colloid Interface Sci.*, 2015, **460**, 264–272.
62 E. Cheng, W. Yin, S. Bai, R. Qiao, Y. Zhong and Z. Li, *Mater. Lett.*, 2015, **146**, 87–90.
63 C. Li, F. Wang, J. Zhu and J. C. Yu, *Appl. Catal., B*, 2010, **100**, 433–439.
64 M. Tou, Y. Mei, S. Bai, Z. Luo, Y. Zhang and Z. Li, *Nanoscale*, 2016, **8**, 553–562.
65 X. Guo, C. Chen, D. Zhang, C. P. Tripp, S. Yin and W. Qin, *RSC Adv.*, 2016, **6**, 8127–8133.
66 X. Guo, W. Song, C. Chen, W. Di and W. Qin, *Phys. Chem. Chem. Phys.*, 2013, **15**, 14681–14688.
67 M. Tou, Z. Luo, S. Bai, F. Liu, Q. Chai, S. Li and Z. Li, *Mater. Sci. Eng., C*, 2017, **70**, 1141–1148.
68 M. Li, Z. Zheng, Y. Zheng, C. Cui, C. Li and Z. Li, *ACS Appl. Mater. Interfaces*, 2017, **9**, 2899–2905.
69 W. Wang, Y. Li, Z. Kang, F. Wang and J. C. Yu, *Appl. Catal., B*, 2016, **182**, 184–192.
70 Q. Tian, W. Yao, Z. Wu, J. Liu, L. Liu, W. Wu and C. Jiang, *J. Mater. Chem. A*, 2017, **5**, 23566–23576.
71 Z. Xu, M. Quintanilla, F. Vetrone, A. O. Govorov, M. Chaker and D. Ma, *Adv. Funct. Mater.*, 2015, **25**, 2950–2960.
72 Q. Tian, W. Yao, W. Wu, J. Liu, Z. Wu, L. Liu, Z. Dai and C. Jiang, *ACS Sustainable Chem. Eng.*, 2017, **5**, 10889–10899.
73 Y. Ma, H. Liu, Z. Han, L. Yang and J. Liu, *J. Mater. Chem. A*, 2015, **3**, 14642–14650.
74 J. Wang, H. Huang, D. Zhang, M. Chen, Y. Zhang, X. Yu, L. Zhou and Q. Wang, *Nano Res.*, 2015, **8**, 2548–2561.
75 W. Deng, F. Xie, H. T. Baltar and E. M. Goldys, *Phys. Chem. Chem. Phys.*, 2013, **15**, 15695–15708.
76 K. Aslan, I. Gryczynski, J. Malicka, E. Matveeva, J. R. Lakowicz and C. D. Geddes, *Curr. Opin. Biotechnol.*, 2005, **16**, 55–62.
77 P. Padhye, S. Sadhu, M. Malik and P. Poddar, *RSC Adv.*, 2016, **6**, 53504–53518.
78 J. Zhang, Y. Huang, L. Jin, F. Rosei, F. Vetrone and J. P. Claverie, *ACS Appl. Mater. Interfaces*, 2017, **9**, 8142–8150.
79 D. Yin, L. Zhang, X. Cao, J. Tang, W. Huang, Y. Han, Y. Liu, T. Zhang and M. Wu, *RSC Adv.*, 2015, **5**, 87251–87258.
80 N. Prakash, D. Thangaraju, R. Karthikeyan, M. Arivanandhan, Y. Shimura and Y. Hayakawa, *RSC Adv.*, 2016, **6**, 80655–80665.
81 P. Huang, W. Zheng, S. Zhou, D. Tu, Z. Chen, H. Zhu, R. Li, E. Ma, M. Huang and X. Chen, *Angew. Chem., Int. Ed.*, 2014, **53**, 1252–1257.
82 S. Zeng, J. Xiao, Q. Yang and J. Hao, *J. Mater. Chem.*, 2012, **22**, 9870–9874.
83 L. Wang, M. Lan, Z. Liu, G. Qin, C. Wu, X. Wang, W. Qin, W. Huang and L. Huang, *J. Mater. Chem. C*, 2013, **1**, 2485–2490.
84 G.-S. Yi and G.-M. Chow, *Chem. Mater.*, 2007, **19**, 341–343.
85 F. Zhang, C.-L. Zhang, H.-Y. Peng, H.-P. Cong and H.-S. Qian, *Part. Part. Syst. Charact.*, 2016, **33**, 248–253.
86 K. Wang, W. Qincheng, F. Wang, S. Bai, S. Li and Z. Li, *Inorg. Chem. Front.*, 2016, **3**, 1190–1197.
87 H. Guan, Y. Sheng, Y. Song, C. Xu, X. Zhou, K. Zheng, Z. Shi and H. Zou, *J. Phys. Chem. C*, 2017, **121**, 23080–23095.
88 H. Li, Q. Huang, Y. Wang, K. Chen, J. Xie, Y. Pan, H. Su, X. Xie, L. Huang and W. Huang, *J. Mater. Chem. C*, 2017, **5**, 6450–6456.
89 Y. Zhu, W. Xu, S. Cui, M. Liu, C. Lu, H. Song and D.-H. Kim, *J. Mater. Chem. C*, 2016, **4**, 331–339.
90 J.-L. Lemyre and A. M. Ritcey, *Chem. Mater.*, 2005, **17**, 3040–3043.
91 G. Murali, R. K. Mishra, J. M. Lee, Y. C. Chae, J. Kim, Y. D. Suh, D.-k. Lim and S. H. Lee, *Cryst. Growth Des.*, 2017, **17**, 3055–3061.
92 G. Murali, S. Kaur, Y. C. Chae, M. Ramesh, J. Kim, Y. D. Suh, D.-K. Lim and S. H. Lee, *RSC Adv.*, 2017, **7**, 24255–24262.
93 H. Qiu, G. Chen, R. Fan, L. Yang, C. Liu, S. Hao, M. J. Sailor, H. Agren, C. Yang and P. N. Prasad, *Nanoscale*, 2014, **6**, 753–757.
94 W. Qin, D. Zhang, D. Zhao, L. Wang and K. Zheng, *Chem. Commun.*, 2010, **46**, 2304–2306.
95 Q.-L. Ye, X. Yang, C. Li and Z. Li, *Mater. Lett.*, 2013, **106**, 238–241.
96 S. Huang, Z. Lou, Z. Qi, N. Zhu and H. Yuan, *Appl. Catal., B*, 2015, **168–169**, 313–321.
97 N. Niu, F. He, S. Gai, C. Li, X. Zhang, S. Huang and P. Yang, *J. Mater. Chem.*, 2012, **22**, 21613–21623.
98 N.-N. Dong, M. Pedroni, F. Piccinelli, G. Conti, A. Sbarbati, J. E. Ramírez-Hernández, L. M. Maestro, M. C. Iglesias-dela Cruz, F. Sanz-Rodriguez, A. Juarranz, F. Chen, F. Vetrone, J. A. Capobianco, J. G. Solé, M. Bettinelli, D. Jaque and A. Speghini, *ACS Nano*, 2011, **5**, 8665–8671.
99 I. Masahiko, G. Christelle, G. Yannick, L. Kheirreddine, F. Tsuguo and B. Georges, *J. Phys.: Condens. Matter*, 2004, **16**, 1501–1521.
100 S. Huang, L. Gu, C. Miao, Z. Lou, N. Zhu, H. Yuan and A. Shan, *J. Mater. Chem. A*, 2013, **1**, 7874–7879.
101 S. Huang, N. Zhu, Z. Lou, L. Gu, C. Miao, H. Yuan and A. Shan, *Nanoscale*, 2014, **6**, 1362–1368.
102 S. Huang, Z. Lou, A. Shan, N. Zhu, K. Feng and H. Yuan, *J. Mater. Chem. A*, 2014, **2**, 16165–16174.
103 S. Huang, Z. Lou, N. Zhu and H. Yuan, *Catal. Commun.*, 2015, **61**, 6–10.
104 S. Huang, H. Wang, N. Zhu, Z. Lou, L. Li, A. Shan and H. Yuan, *Appl. Catal., B*, 2016, **181**, 456–464.
105 X. Liu, W. Di and W. Qin, *Appl. Catal., B*, 2017, **205**, 158–164.
106 M. Haase and H. Schafer, *Angew. Chem., Int. Ed.*, 2011, **50**, 5808–5829.

107 D. L. Dexter, *J. Chem. Phys.*, 1953, **21**, 836–850.
108 J. Tang, Y. Zhang, J. Gou, Z. Ma, G. Li, Y. Man and N. Cheng, *J. Alloys Compd.*, 2018, **740**, 229–236.
109 S. Som and S. K. Sharma, *J. Phys. D: Appl. Phys.*, 2012, **45**, 415102.
110 E. W. Barrera, M. C. Pujol, F. Diaz, S. B. Choi, F. Rotermund, K. H. Park, M. S. Jeong and C. Cascales, *Nanotechnology*, 2011, **22**, 075205.
111 Z. E. Liu, J. Wang, Y. Li, X. Hu, J. Yin, Y. Peng, Z. Li, Y. Li, B. Li and Q. Yuan, *ACS Appl. Mater. Interfaces*, 2015, **7**, 19416–19423.
112 J. Leng, J. Chen, D. Wang, J.-X. Wang, Y. Pu and J.-F. Chen, *Ind. Eng. Chem. Res.*, 2017, **56**, 7977–7983.
113 L. Chen, F. He, C. Shi, C. He, E. Liu, L. Ma and N. Zhao, *J. Alloys Compd.*, 2018, **740**, 719–726.
114 T. Li, S. Liu, H. Zhang, E. Wang, L. Song and P. Wang, *J. Mater. Sci.*, 2010, **46**, 2882–2886.
115 H. Zhou, S. Xu, D. Zhang, S. Chen and J. Deng, *Nanoscale*, 2017, **9**, 3196–3205.
116 D. Yin, F. Zhao, L. Zhang, X. Zhang, Y. Liu, T. Zhang, C. Wu, D. Chen and Z. Chen, *RSC Adv.*, 2016, **6**, 103795–103802.
117 Y. Liu, D. Wang, J. Shi, Q. Peng and Y. Li, *Angew. Chem., Int. Ed.*, 2013, **52**, 4366–4369.
118 Z. Wu, S. Yang and W. Wu, *CrystEngComm*, 2016, **18**, 2222–2238.
119 S. Yang, B. Zhou, Z. Ding, H. Zheng, L. Huang, J. Pan, W. Wu and H. Zhang, *J. Power Sources*, 2015, **286**, 124–129.
120 S. Obregon and G. Colon, *Chem. Commun.*, 2012, **48**, 7865–7867.
121 L. Shan and Y. Liu, *J. Mol. Catal. A: Chem.*, 2016, **416**, 1–9.
122 S. Ganguli, C. Hazra, M. Chatti, T. Samanta and V. Mahalingam, *Langmuir*, 2016, **32**, 247–253.
123 K. Fu, J. Huang, N. Yao, X. Xu and M. Wei, *Ind. Eng. Chem. Res.*, 2015, **54**, 659–665.
124 C. Regmi, Y. K. Kshetri, S. K. Ray, R. P. Pandey and S. W. Lee, *Appl. Surf. Sci.*, 2017, **392**, 61–70.
125 S. Obregon, S. W. Lee and G. Colon, *Dalton Trans.*, 2014, **43**, 311–316.
126 P. M. Martins, V. Gomez, A. C. Lopes, C. J. Tavares, G. Botelho, S. Irusta and S. Lanceros-Mendez, *J. Phys. Chem. C*, 2014, **118**, 27944–27953.
127 S. Huang, Y. Feng, L. Han, W. Fan, X. Zhao, Z. Lou, Z. Qi, B. Yu and N. Zhu, *RSC Adv.*, 2014, **4**, 61679–61686.
128 M. Samadi, M. Zirak, A. Naseri, E. Khorashadizade and A. Z. Moshfegh, *Thin Solid Films*, 2016, **605**, 2–19.
129 C. Wang, Y. Ao, P. Wang, J. Hou and J. Qian, *Appl. Surf. Sci.*, 2010, **257**, 227–231.
130 A.-W. Xu, Y. Gao and H.-Q. Liu, *J. Catal.*, 2002, **207**, 151–157.
131 M. Wang, Y. Che, C. Niu, M. Dang and D. Dong, *J. Hazard. Mater.*, 2013, **262**, 447–455.
132 K. T. Ranjit, I. Willner, S. H. Bossmann and A. M. Braun, *Environ. Sci. Technol.*, 2001, **35**, 1544–1549.
133 A. S. Weber, A. M. Grady and R. T. Koodali, *Catal. Sci. Technol.*, 2012, **2**, 683.
134 Q. Tian, W. Wu, S. Yang, J. Liu, W. Yao, F. Ren and C. Jiang, *Nanoscale Res. Lett.*, 2017, **12**, 221.
135 K. T. Ranjit, H. Cohen, I. Willner, S. Bossmann and A. M. Braun, *J. Mater. Sci.*, 1999, **34**, 5273–5280.
136 W. Choi, A. Termin and M. R. Hoffmann, *J. Phys. Chem.*, 1994, **98**, 13669–13679.
137 K. M. Parida and N. Sahu, *J. Mol. Catal. A: Chem.*, 2008, **287**, 151–158.
138 J. Choi, H. Park and M. R. Hoffmann, *J. Phys. Chem. C*, 2010, **114**, 783–792.
139 D. Xu, L. Feng and A. Lei, *J. Colloid Interface Sci.*, 2009, **329**, 395–403.
140 A. Khataee, R. Darvishi Cheshmeh Soltani, Y. Hanifehpour, M. Safarpour, H. Gholipour Ranjbar and S. W. Joo, *Ind. Eng. Chem. Res.*, 2014, **53**, 1924–1932.
141 K. Feng, S. Huang, Z. Lou, N. Zhu and H. Yuan, *Dalton Trans.*, 2015, **44**, 13681–13687.
142 J. Méndez-Ramos, P. Acosta-Mora, J. C. Ruiz-Morales, M. Sierra, A. Redondas, E. Ruggiero, L. Salassa, M. E. Borges and P. Esparza, *Opt. Mater.*, 2015, **41**, 98–103.
143 J. C. Boyer and F. C. van Veggel, *Nanoscale*, 2010, **2**, 1417–1419.
144 X. Liu and M. T. Swihart, *Chem. Soc. Rev.*, 2014, **43**, 3908–3920.
145 W. Liu, Q. Xu, W. Cui, C. Zhu and Y. Qi, *Angew. Chem., Int. Ed.*, 2017, **56**, 1600–1604.
146 K. Manthiram and A. P. Alivisatos, *J. Am. Chem. Soc.*, 2012, **134**, 3995–3998.
147 A. Agrawal, S. H. Cho, O. Zandi, S. Ghosh, R. W. Johns and D. J. Milliron, *Chem. Rev.*, 2018, **118**, 3121–3207.
148 D. Zhou, D. Liu, W. Xu, Z. Yin, X. Chen, P. Zhou, S. Cui, Z. Chen and H. Song, *ACS Nano*, 2016, **10**, 5169–5179.
149 Z. Zhang, Y. Liu, Y. Fang, B. Cao, J. Huang, K. Liu and B. Dong, *Adv. Sci.*, 2018, 1800748.
150 X. Xie, Z. Li, Y. Zhang, S. Guo, A. I. Pendharkar, M. Lu, L. Huang, W. Huang and G. Han, *Small*, 2017, **13**, 1602843.
151 Y. Chen, C. Lu, L. Tang, S. Wei, Y. Song and J. Wang, *Sol. Energy Mater. Sol. Cells*, 2016, **149**, 128–136.
152 J. Hong, Z. S. Hong, X. Cheng, C. W. Bo, W. J. Chen, L. X. Feng and Q. J. Rong, *Adv. Energy Mater.*, 2015, **5**, 1401041.